Original Research Article

Ferroptosis-Associated Extracellular Matrix Remodeling in Radiation-Induced Lung Fibrosis Progression

Dose-Response:
An International Journal
July-September 2024:1–12

DOI: 10.1177/15593258241289829
journals.sagepub.com/home/dos
Sage

Xinyu Yan[1,2], Peixuan Yang[1,2], Chen Yang[1,2], Yinghui Wang[3], Zhijun Feng[3], Ting Liu[2], Yani Li[2], Cheng Zhou[4], and Minying Li[2]

Abstract

Background: Radiation-induced lung fibrosis (RILF) is a life-threatening complication of thoracic radiotherapy. Ferroptosis, a recently discovered type of cell death, is believed to contribute to RILF, though the associated mechanisms are unknown. This study aimed to investigate the potential mechanism of ferroptosis in RILF and examine the contribution of different cell types to ferroptosis during RILF progression. **Methods:** Histopathological changes in RILF lung tissue were assessed through H&E and Masson staining. IHC staining investigated ferroptosis markers (GPX4, ACSL4, NCOA4). Ferroptosis-related genes (FRG) and pathway scores were derived from RILF transcriptome microarray data. The sc-RNAseq analysis detected FRG score dynamics across cell types, validated by IF staining for PDGFR-α and ACSL4. **Results:** ACSL4 and NCOA4 protein levels were significantly higher and GPX4 lower in IR than control. FRG scores were positively correlated with fibrosis-related pathway scores in the RILF transcriptome data. FRG and ECM scores were concurrently upregulated in myofibroblasts. Enhanced co-staining of PDGFR-α and ACSL4 were observed in the fibrotic areas of RILF lungs. **Conclusions:** Our research indicated that in RILF, fibroblasts undergoing ferroptosis may release increased levels of ECM, potentially accelerating the progression of lung fibrosis. This finding presents ferroptosis as a potential therapeutic target in RILF.

Keywords

radiation-induced lung fibrosis, ferroptosis, fibroblasts, scRNAseq

Introduction

Radiation-induced lung injury (RILI) is a common complication of radiotherapy for thoracic tumors. The incidence of RILI varies between 5% and 25% among patients with thoracic tumors who undergo curative radiotherapy.[1-4] X-ray irradiation induces cellular DNA damage and oxidative stress, initiating an inflammatory response and subsequent tissue reorganization. This process represents the regeneration or restoration of organ function. Nevertheless, the extent of

[1] Zhongshan City People's Hospital, Xinxiang Medical University, Xinxiang, China
[2] Department of Radiation Oncology, Zhongshan City People's Hospital, Zhongshan, China
[3] Department of Radiation Medicine, Guangdong Provincial Key Laboratory of Tropical Disease Research, NMPA Key Laboratory for Safety Evaluation of Cosmetics, School of Public Health, Southern Medical University, Guangzhou, China
[4] Department of Radiation Oncology, Nanfang Hospital, Southern Medical University, Guangzhou, China

Received 23 February 2024; accepted 5 September 2024

Corresponding Authors:
Cheng Zhou, Department of Radiation Oncology, Nanfang Hospital, Southern Medical University, 1838 Guangzhou Avenue North, Guangzhou, 510515, China
Email: czhou.rob@gmail.com

Minying Li, Department of Radiation Oncology, Zhongshan City People's Hospital, No.2 Sunwen Middle Road, Zhongshan City 528403, China.
Email: lmy.69@163.com

radiation-induced lung injury (RILI) in patients can vary depending on the dose of X-rays received and the sensitivity of the lung tissue to radiation. Some individuals develop varying degrees of radiation-induced pneumonitis or pulmonary fibrosis (RILF). This condition is characterized by the activation of fibroblasts, their transformation into myofibroblasts, hypoxia, and secretion of extracellular matrix, contributing to tissue remodeling.[3,5] Structural remodeling of lung tissue ultimately results in increased stiffness of the lung parenchyma and thickening of the alveolar walls. This progression ultimately leads to lung failure, severely affecting quality of life.[6]

Ferroptosis is an iron-dependent form of regulated cell death, distinguished by an imbalance in cellular metabolism resulting from iron overload, lipid peroxidation, and accumulation of reactive oxygen species (ROS).[7] Certain studies have documented the existence of ferroptosis in RILF and have demonstrated the potential to mitigate fibrosis severity through the utilization of Fer-1, an inhibitor of iron-dependent cell death.[8-11] However, the specific cellular mechanisms underlying the promotion of fibrosis following ferroptosis remain unclear and require further investigation.

At the cellular level, exposure to pro-fibrogenic doses of irradiation induces apoptosis, senescence, cytokine secretion, and transformations, which have the potential to affect various cellular components.[12] The popularity and maturity of transcriptome and single-cell RNA sequencing (sc-RNAseq) technologies make them powerful tools for studying changes in RILF transcript levels. Our study started with the analysis of transcriptome microarray data from a mouse model of RILF, carrying out differential and enrichment analyses to understand the metabolic pathway changes. Further, we utilized sc-RNAseq data to examine significant alterations within the framework of the single-cell transcriptome in RILF. Our research offers fresh insights into the development of RILF and provides additional evidence that ferroptosis plays a critical role in this disease.

Materials and methods

Mouse Model of Radiation Injury

Female C57BL/6J mice, aged 8-10 weeks and weighing 20 ± 2 g, were obtained from Guangdong Medical Laboratory Animal Center (SYXK 2021-0167). A total of 24 mice were randomly assigned to either the control or irradiation (IR) group. Prior to thoracic irradiation, mice were anesthetized with an intraperitoneal injection of 8 mL/kg 4% hydration solution. In the IR group, X-ray irradiation was delivered with a single dose of 17 Gy using a 6 MeV Artist Linac (Siemens, Munich, Germany) at a dose rate of 3 Gy/min. Conversely, the control group underwent identical procedures, without an additional irradiation step. Lung tissues were collected from mice 20 weeks after radiation exposure.

Transcriptome Microarray Sequencing

Twenty weeks post-irradiation, all mice were euthanized by cervical dislocation. Fresh lung tissues were extracted and treated with TRIzol reagent (Thermo Fisher Scientific, Waltham, MA, USA). RNA was extracted using the RNeasy Mini Kit (Qiagen, Hilden, Germany), and DNA contamination was subsequently removed by DNase I treatment (Qiagen, Venlo, The Netherlands). The resulting RNA was purified using nuclease-free water and stored at −80°C in a refrigerator for future use. The RNA concentration was determined using a 2100 Bioanalyzer system (Agilent Technologies, Santa Clara, CA, USA) to confirm sample integrity and purity. Gene expression was detected using a transcriptome microarray (Mouse Sentrix-6 V2 Whole Genome Bead Chip, BD-201-0202; Illumina, Inc., San Diego, CA, USA). By analyzing the signals processed by the built-in processing chip, the system generates original expression files and subsequently conducts gene annotations.

Transcriptome Microarray Data Analysis

Raw data were processed using R software (version 4.3.1) to generate gene expression matrices. For data background correction, normalization, summarizing, and reporting of differentially expressed genes (DEGs), the Limma (V3.54.0)[13] package was used. The threshold for DEGs was set at $P < 0.05$, with an absolute magnitude of log2 fold change (log2(FC)) ≤ 0.5 after log2 transformation of expression data. This process identified genes in the mouse lungs that exhibited differential expression after X-ray irradiation. Cluster analysis of these DEGs was performed using the pheatmap (1.0.12) package to analyze expression patterns after irradiation. The upregulated portions of these DEGs were subjected to Gene Ontology (GO)[14-17] and Kyoto Encyclopedia of Genes and Genomes (KEGG)[18-20] enrichment analyses using the clusterProfiler package (V4.6.0)[21] with the significance threshold set at $P < 0.05$. The results were visually represented using the ggplot2 package (V3.4.3).

Data Acquisition

The RILI datasets GSE41789[22] and GSE211713[12] were downloaded from the Gene Expression Omnibus (GEO) database (https://www.ncbi.nlm.nih.gov/geo/). GSE41789, collected from the GPL1261 platform (Affymetrix Mouse Genome 430 2.0 Array), comprises 45 mouse lung tissue samples (10-week-old female C57Bl/Ncr mice) with or without irradiation in an age-matched cohort. For subsequent analyses, the 30-week time point after irradiation, dose of 17.5 Gy (IR 17.5 Gy), and control group were selected. The sc-RNAseq dataset GSE211713 was generated using the Illumina NovaSeq 6000 and GPL24247 platforms. For further analysis, data from the 17 Gy dose (IR17 Gy) and control groups were selected.

Single-Cell RNA-seq Data Processing

The Seurat (V4.3.0) package[20] was used to process raw data from single cells. In the quality control steps, the following genes or cells were filtered out: (a) nCounts <200; (b) nFeatures >6000; (c) cells with >15% of mitochondrial genes. We used the Harmony R package for batch correction before subclustering analysis. Then, principal components (PCs) were constructed using highly variable genes, and the first 20 PCs were selected for graph-based clustering using FindNeighbors in Seurat. To visualize the clustering analysis, t-distributed Stochastic Neighbor Embedding (t-SNE) was performed using the RunTSNE function in Seurat. Finally, cells were clustered using FindClusters based on the default Seurat parameters, with the resolution parameter set to 0.3.

Gene Signature Scores for Specific Functions

We utilized gene sets from MsigDB[23] to compute the ssGSEA score through the computational single-sample genome enrichment analysis (ssGSEA) function in the GSVA package,[24] enabling the comparison of changes in metabolic pathways between samples. Gene signatures related to oxidative stress, collagen metabolism, fibrosis regulation, iron metabolism, lipid metabolism, glutathione metabolism, and extracellular matrix synthesis were obtained from previous studies and stored in MsigDB. The gene sets used to calculate the ferroptosis-related gene (FRG) scores were obtained from the KEGG database (https://www.genome.jp/kegg/; Supplemental Table 3). Employing the aforementioned gene sets and applying the AddModuleScore function from the Seurat package, we computed scores for the scRNA-seq analyses, which revealed metabolic changes in various cell clusters.

Hematoxylin and Eosin (H&E) and Masson's Staining

Lung tissues obtained from the mice were fixed in 4% paraformaldehyde for 24 h, followed by dehydration with graded ethanol. Subsequently, the tissues were embedded in paraffin using standard procedures and cut into sections of 4 μm thickness. Hematoxylin and eosin (H&E) staining was performed for 5 min after dewaxing and hydration using H&E reagents (G1076; Servicebio, Wuhan, China). Masson's trichrome staining was performed using a staining kit (G1006; Servicebio). Stained tissues were examined under a microscope (Carl Zeiss AG, Wetzlar, Germany) at ×400 magnification.

Immunofluorescence Staining

Paraffin-embedded sections of mouse lung tissue were treated with glutaraldehyde and anhydrous ethanol. Following gradient dewaxing through the standard process, a 30-minute repair was conducted using Tris-EDTA antigen repair solution in a 95°C water bath. Co-staining for acyl-CoA synthetase long-chain family member 4 (ACSL4; 1:500, DF12141; Affinity Biosciences, Cincinnati, OH, USA) and platelet-derived growth factor receptor alpha (PDGFR-α; 1:1000, P16234; Cell Signaling Technology, Danvers, MA, USA) was carried out utilizing a Three-color mIHC Fluorescence kit (Recordbio Biological Technology, Shanghai, China) based on tyramide signal amplification technology following the manufacturer's instructions. Nuclei were counterstained with 4′,6-diamidino-2-phenylindole (DAPI) for 10 min. Stained tissues were examined under a microscope (Carl Zeiss AG) at ×400 magnification.

IHC Staining

Immunohistochemical staining was performed to determine the expression levels of the following well-known ferroptosis markers in the lung sections: anti-ACSL4 (1:1000, #DF12141; Affinity Biosciences), anti-GPX4 (1:1000, #A5569; Selleck, Houston, TX, USA), and anti-NCOA4 (1:1000, #DF4255; Affinity Biosciences). Paraffin-embedded sections of mouse lung tissue were prepared according to standard protocols. They were initially deparaffinized to water using a deparaffinizing solution and ethanol gradient, and antigen repair was then performed using a Tris-EDTA solution. This was followed by blocking endogenous peroxidase activity using a 3% hydrogen peroxide solution. After being sealed with BSA, the sections were incubated overnight with primary antibodies and subsequently with horseradish peroxidase-labeled secondary antibodies. Phosphate buffered saline (PBS) was used instead of the primary antibody as a negative control, and a known positive specimen was used as a positive control. Stained tissues were examined under a microscope (Carl Zeiss AG) at ×400 magnification.

Results

Enrichment Analysis of Ferroptosis in RILF

Using methods as previously described,[25] we established an RILF mouse model to study the molecular mechanisms underlying RILF occurrence. Compared with the control group, the mice displayed notable signs of pulmonary fibrosis 20 weeks after a single 17 Gy X-ray irradiation. These included thickening of the alveolar walls, increased secretion of the extracellular matrix, and increased deposition of collagen fibers, in addition to the formation of solid fibrotic masses visible in some lung tissues (Figure 1(A)).

Examination of transcriptome microarray data demonstrated that when considering all genes in this study, principal component analysis effectively differentiated between the IR and control groups with a high level of accuracy (Figure 1(B)). Compared to expression levels in the control group, there were 519 upregulated and 355 downregulated DEGs after irradiation (Figure 1(C)). The expression patterns of these DEGs are

visually represented in a heatmap (Figure 1(D)). A detailed list of the DEGs can be found in Supplemental Table 1.

To enhance our understanding of the metabolic changes within RILF, we conducted KEGG and GO enrichment analyses on the DEGs upregulated in response to ionizing radiation. The KEGG results revealed that representative pathways were significantly enriched in various categories, including respiratory system diseases ("Asthma," "Pertussis," etc.), DNA damage and repair ("Nucleotide excision repair," "Amino sugar and nucleotide sugar metabolism," etc.), and immune and inflammatory responses ("Antigen processing and presentation," 'C-type lectin receptor signaling pathway," "Complement and coagulation cascades," etc.). The representative pathways identified in the GO results were enriched in extracellular matrix and fibrogenesis ("extracellular matrix binding," "collagen-containing extracellular matrix," "fibrillar collagen trimer," etc.), glutathione metabolism ("glutathione transferase activity," "glutathione peroxidase activity"), iron metabolism ("regulation of metal ion transport"), and mitochondrial damage ("mitochondrial protein-containing complex," "mitochondrial large ribosomal subunit," etc.) (Figure 1(E), Supplemental Table 2). These results are consistent with previously reported findings.[26-29] Intriguingly, oxidative stress, reactive oxygen species (ROS), glutathione metabolism, iron ion metabolism, and mitochondrial damage were strongly associated with ferroptosis. This suggests the emergence of ferroptosis in RILF.

FRG Score Establishment and IHC Staining for Ferroptosis

After detecting modifications in the ferroptosis pathway in the enrichment results, we sought evidence of ferroptosis in RILF. Ferroptosis, a recognized mechanism of regulated cell death, is characterized by iron dependence and dysregulated lipid peroxidation in cell membranes. To assess the manifestation of ferroptosis in the mouse lung tissue following irradiation, we conducted a comprehensive search of MSigDB for gene sets associated with iron metabolism, lipid metabolism, glutathione metabolism, and oxidative stress. Subsequently, the acquired data were scored using ssGSEA. The resulting heatmap of scores revealed a substantial increase in the metabolic pathways linked to ferroptosis after irradiation (Figure 2(A) and (C)).

Employing the ssGSEA scoring tool, we generated the FRG score using a list of genes associated with the ferroptosis pathway in the KEGG database. The FRG score was significantly increased in the IR group. Additionally, consistent outcomes were observed when the same scoring technique was applied to the GSE41789 dataset[22] (Figure 2(D) and (E)). Paraffin-embedded sections of mouse lung tissue were subjected to IHC staining for ferroptosis markers, including ACSL4, glutathione peroxidase 4 (GPX4), and NCOA4.[30-34] Following radiation exposure, the results demonstrated changes consistent with ferroptosis were observed, including a decrease in GPX4 expression and an increase in the expression of ACSL4 and nuclear receptor coactivator 4 (NCOA4) (Figure 2(F)). This underscores the credibility of our FRG score and provides evidence that alterations associated with ferroptosis occur in mouse lung tissue following irradiation.

Positive Correlations Between FRG and Fibrosis-Related Pathway Scores

After confirming the presence of ferroptosis in RILF, we investigated the interconnection between ferroptosis and fibrosis-associated pathways. Using MSigDB, we conducted a thorough search for gene sets related to collagen metabolism, fibrosis regulation, extracellular matrix (ECM) synthesis, and angiogenesis. Following scoring of these gene sets, discernible alterations were observed in the IR group. Notably, pathways associated with collagen metabolism, fibrosis regulation, and ECM synthesis were augmented, along with a concurrent reduction in the pathways linked to angiogenesis (Figure 3(A) and (B)). These findings imply that pathways associated with fibrosis were activated in mouse lung tissue after exposure to X-ray radiation. Subsequently, correlation analyses were performed to examine the relationship between the FRG score and the scores of lung fibrosis-related pathways. The results revealed a significant positive correlation between the FRG scores and scores associated with Collagen Metabolism, Fibrosis Regulation, and Extracellular Matrix Synthesis. Additionally, a negative correlation was observed between the FRG score and Angiogenesis (Figure 3(C)). These findings suggest a positive correlation between ferroptosis and IR-induced pulmonary fibrosis.

FRG Score Increases in Epithelial Cells and Fibroblasts

Using microarray data from both RILF and lung tissue, we identified a correlation between ferroptosis and fibrosis. However, the cells in which ferroptosis plays a predominant role in promoting fibrosis remain unclear. To address this, we acquired and analyzed scRNA-seq data (GSE211713) for RILF. Using conventional markers, we successfully categorized the dataset into four main cell types: endothelial cells (Car4, Gpihbp1, and Pecam1), fibroblasts (Mfap4 and Col1a1), immune cells (Ptprc), and epithelial cells (Epcam and Dynlrb2) (Figure 4(A) and (B), Supplemental Figure 1). In the IR group, both the proportion and quantity of immune cells increased, accompanied by a decrease in the proportion of endothelial and epithelial cells. In addition, the number of fibroblasts increased slightly (Figure 4(C)). These trends are consistent with previously reported findings.[35]

The FRG scores for all cells were computed. In the IR group, a notable overall increase in FRG score was observed. Notably, the Epithelial and Fibroblast FRG scores displayed relatively large Cohen's d values (d = 0.327, 0.275), indicating

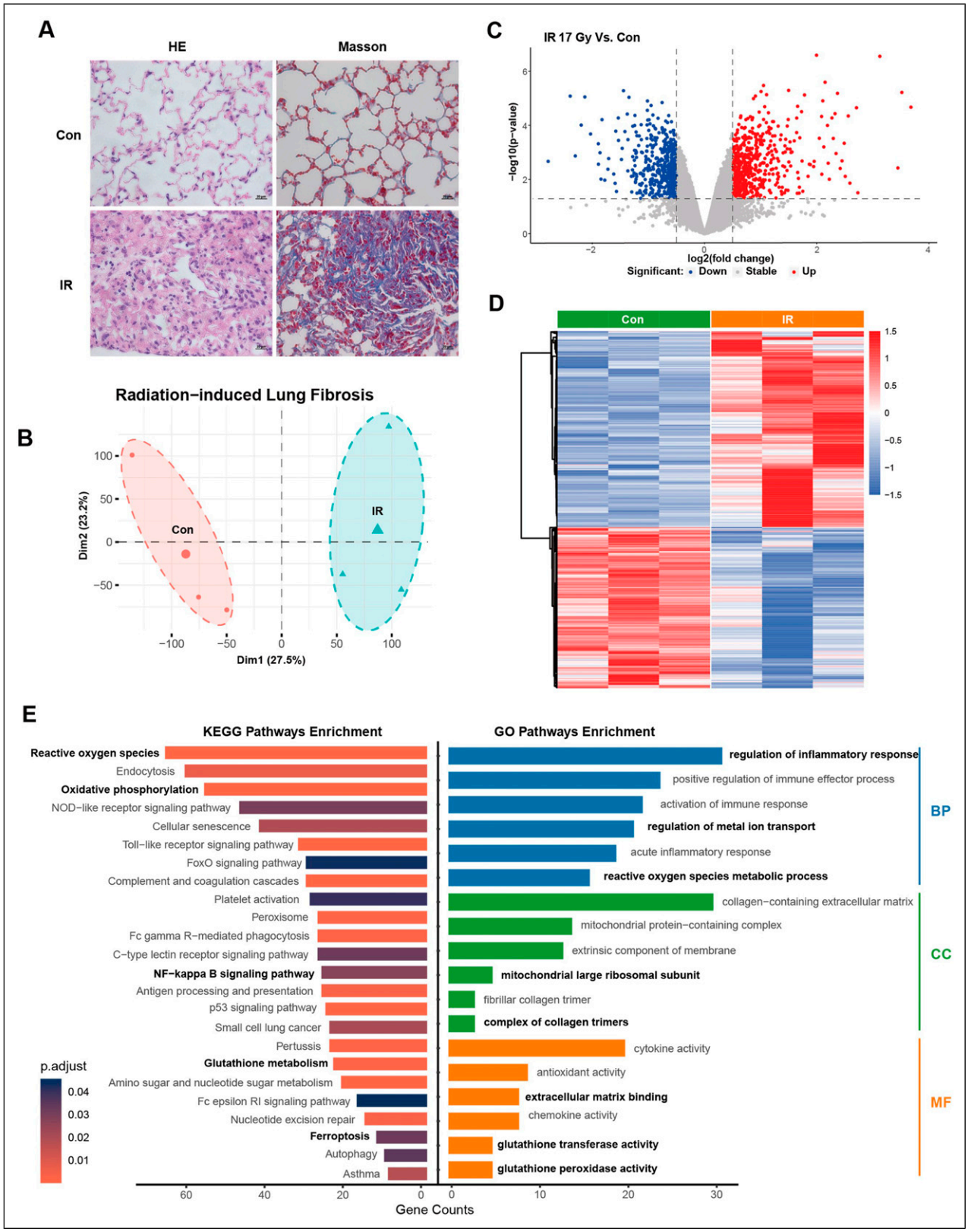

Figure 1. Establishment of mouse RILF model and analysis of transcriptome microarray data analysis. (A) HE and masson staining of lung tissue collected at 20 weeks after IR (control, 17 Gy). Lungs treated to 17 Gy dose irradiation develop foci of fibrosis. Collagen: blue; cytoplasm/epithelia: pink. Scale bar = 20 μm. (B) The PCA plot of the distribution status of the two groups (C) Volcano plots displaying significantly differentially expressed genes. $|\log2FC| \geq 0.5$ and $P < 0.05$. (D) Heatmap displaying the expressions of the DEGs. Blue corresponds to lower gene expression and red to higher gene expression. (E) Bar plot of enriched KEGG pathways/GO terms showing DEGs.

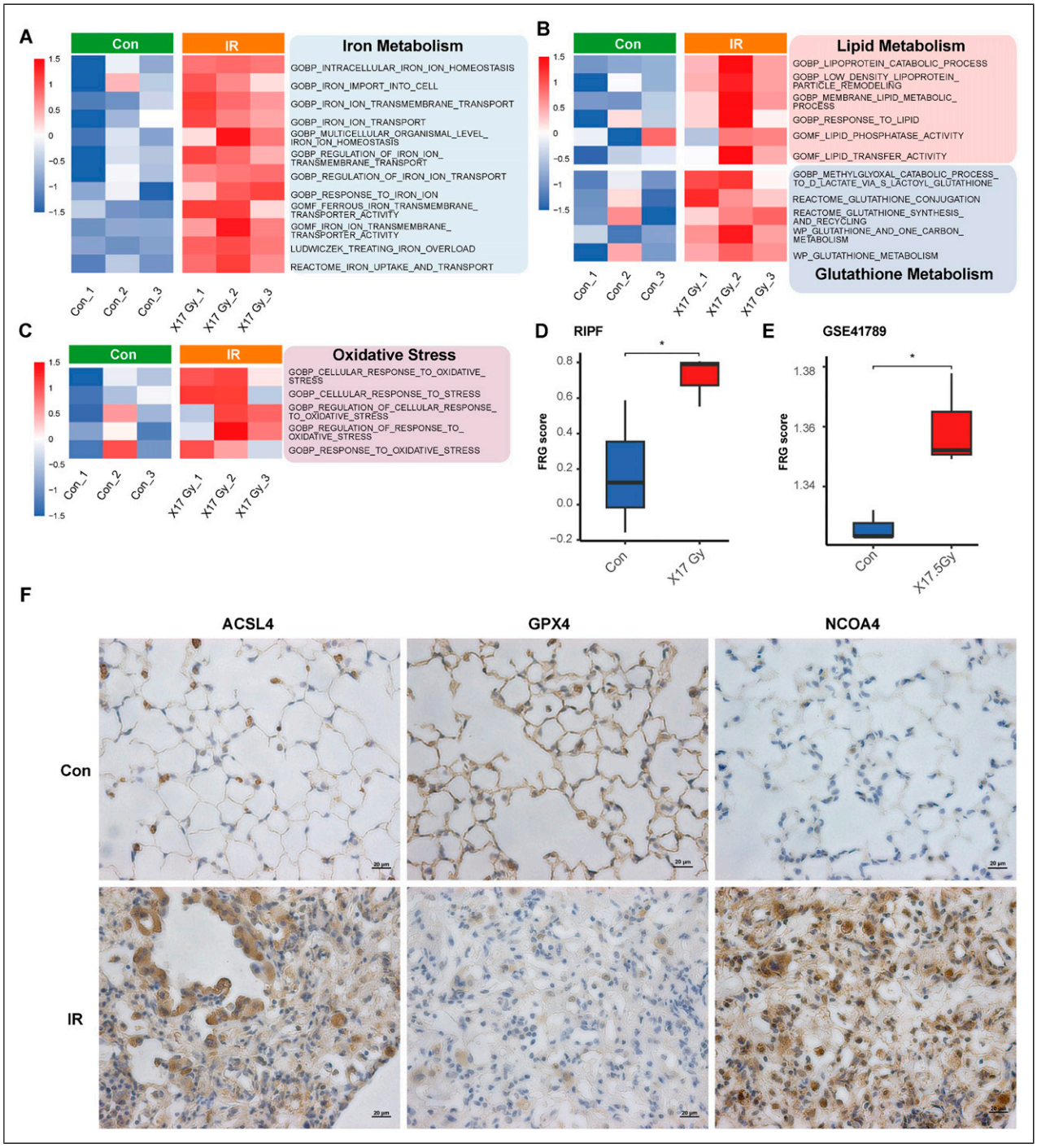

Figure 2. Validation of FRG scores and IHC in RIPF. (A-C) Use ssGSEA to score pathways related to ferroptosis, and display the scores in a heatmap based on their magnitudes. (A) Iron metabolism. (B) Lipid metabolism and glutathione metabolism (C) Oxidative stress. Blue corresponds to lower and red to higher. (D-E) FRG score in RIPF and GSE41789 (n = 3). *$P < 0.05$. (F) Representative IHC images of ACSL4, GPX4 and NCOA4 in the lung sections. IHC staining of lung tissue collected at 20 weeks after IR (control, 17 Gy). Lungs treated to 17 Gy dose irradiation develop foci of fibrosis. Scale bar = 20 μm.

a more pronounced increase. This suggests that ferroptosis is particularly pronounced in these two cell types in RILF.

Previous studies have examined ferroptosis in epithelial cells.[8-11] For instance, Li et al explored ferroptosis in RILI using the BEAS-2B cell model and demonstrated that the induction of ferroptosis in epithelial cells contributed to the onset of RILF. Notably, the administration of Fer-1 alleviated fibrotic progression associated with RILF.[11]

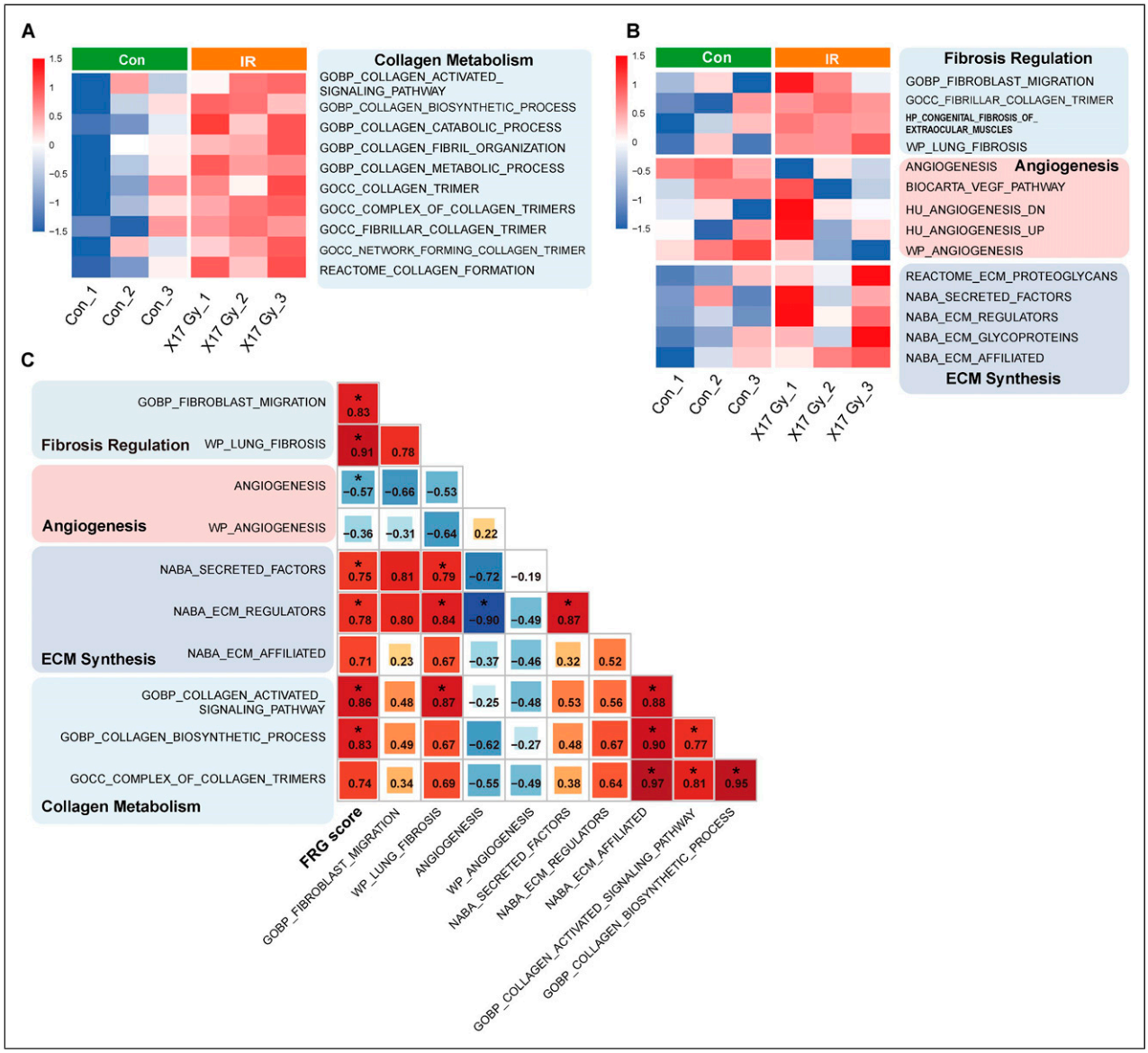

Figure 3. (A-B) Use ssGSEA to score pathways related to collagen metabolism, fibrosis regulation, ECM synthesis, and angiogenesis, and display the scores in a heatmap based on their magnitudes. Blue corresponds to lower and red to higher. (C) Correlation heatmap showing the correlation between FRG score and pathways in AB. Blue represents negative correlation and red represents positive correlation.

Ferroptosis in fibroblasts had not previously been documented in the context of RILF. Consequently, we focused on investigating ferroptosis specifically in fibroblasts during RILF.

Positive Correlation Between FRG and ECM Scores

Using scRNA-seq data, we extracted fibroblasts and conducted a dynamic comparison of their FRG scores. At the time points 1 and 2 months after radiation, no discernible differences were observed in the FRG scores between the IR and control groups. Nevertheless, the changes became noticeably large in the later phase, especially at the time points 3, 4, and 5 months post-irradiation (Figure 5(A)). We selected a time point of 5 months (17-21 weeks) for subsequent investigations.

The disparity in FRG scores compared to those of the controls was more pronounced (d = 0.545) in fibroblasts 4 and 5 months post-irradiation (Figure 5(B)). Following previous descriptions, we categorized fibroblasts into five distinct subgroups: Fibro_Col13a (Col13a1+, Tcf21+), Fibro_Col13a (Col14a1+, Pi16+, Meg3+), Fibro_Sftc (Sftc+, Pdgfrb+), myofibroblasts (Hhip+, Cdh11+, Pdgfrb+), and SMC (Myh11, Acta2) (Figure 5(C) and (E)).

Fibroblasts with higher FRG scores were primarily composed of myofibroblasts, Fibro_col13a, and Fibro_col14a. Similarly, these three cell types were associated with lipid and iron metabolism (Figure 5(G), Supplemental Figure 2(A) and 2(B)).

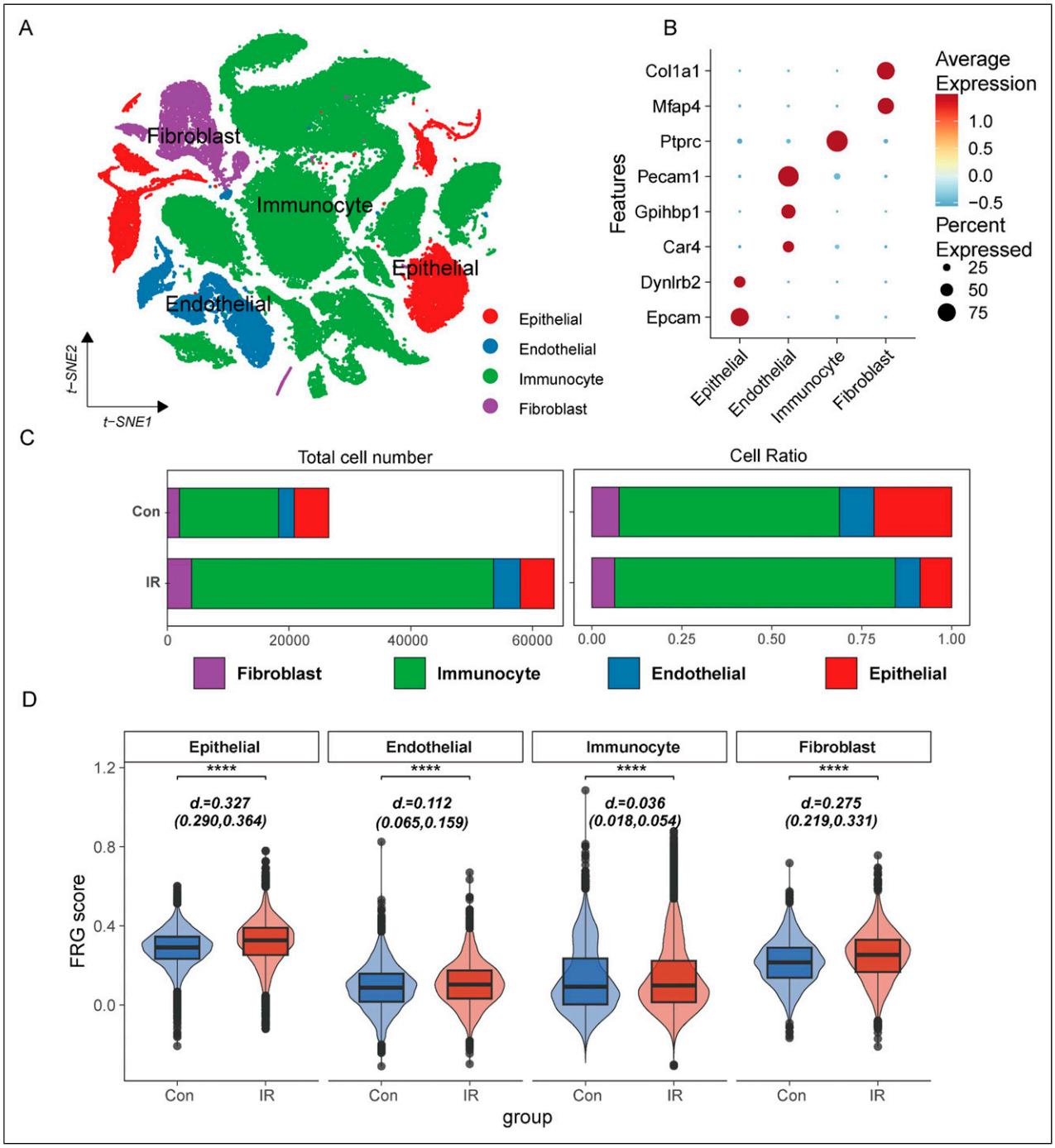

Figure 4. Single-cell RNAseq FRG scores in different cell types. (A) tSNE visualization of 90069 cells from 15 different samples (5 Con; 10 IR17 Gy, two per time point) annotated by cell type. (B) Dot plot of the expression of the markers used for cell type identification. (C) Dynamics in cell proportions of the epithelial, endothelial, immunocyte and fibroblast cells across Con and IR. (D) FRG score in different cell types before and after irradiation. To compare two groups, the *P* value was computed with the Wilcoxon test (two-sided test) from ggpubr (n/s, $P > 0.05$; *, $P < 0.05$; **, $P < 0.01$; ***, $P < 0.001$; ****, $P < 0.0001$).

This implies that these three cell types constitute the predominant fraction of cells involved in ferroptosis. To quantify the capacity of fibroblasts to secrete the ECM, we used the ECM score derived from MSigDB (Figure 5(H), Supplemental Figure 2(C)). After irradiation, the ECM scores of myofibroblasts Fibro_col13a and Fibro_col14a significantly increased (d = 0.324) (Figure 5I).

These results imply that ferroptotic fibroblasts showed increased ECM-secreting activity after irradiation. To validate this, we performed dual-color immunofluorescence staining

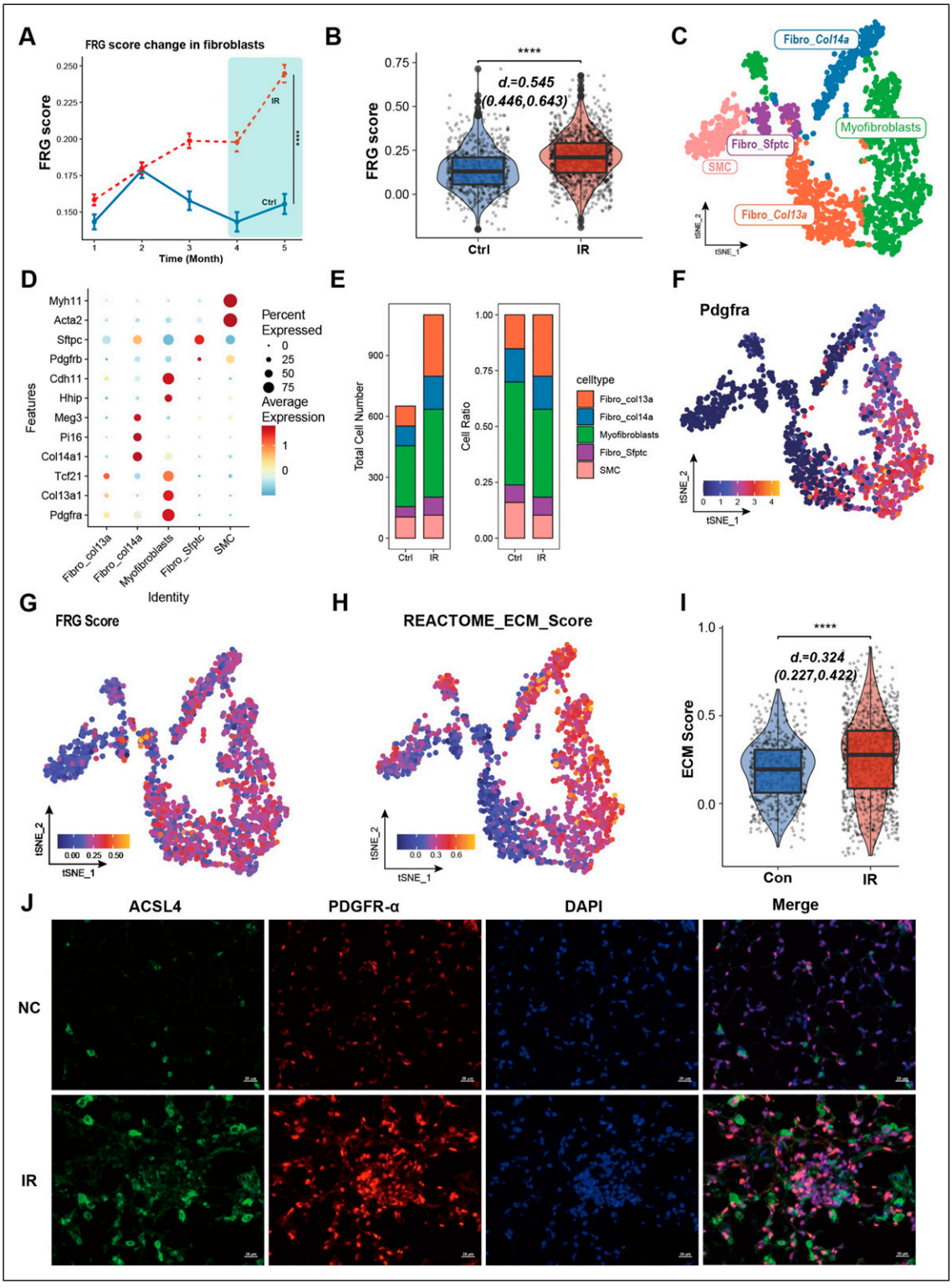

Figure 5. Ferroptosis and ECM dynamics in fibroblast. (A) Dynamics of FRG score in fibroblast at different time points. (B) FRG score changes in fibroblast at 4-5 month after IR. (C) tSNE visualization of 1752 cells from 6 different samples (2 Con; 4 IR17 Gy, two per time point) annotated by cell type. (D) Dot plot of the expression of the markers used for fibroblast subsets identification. (E) Dynamics in subsets cell proportions of the of fibroblasts across Con and IR. (F) Tsne visualization of the expression of Pdgfra. (G-H) Tsne visualization of the distribution of FRG score and ECM score. (I) ECM score in fibroblast before and after irradiation at 4-5 month. To compare two groups, the *P* value was computed with the Wilcoxon test (two-sided test) from ggpubr (n/s, $P > 0.05$; *, $P < 0.05$; **, $P < 0.01$; ***, $P < 0.001$; ****, $P < 0.0001$). J) Representative plots of immunofluorescence staining of ACSL4 and PDGFR-α in RIPF paraffin sections. Scale bar = 20 μm.

on paraffin-embedded mouse lung tissue sections using anti-PDGFRα and anti-ACSL4. PDGFR-α is a marker for enhanced fibroblast activity,[36] while ACSL4 is a marker for ferroptosis.[33,34] The results revealed an increase in dual-color co-staining in the fibrotic areas after irradiation (Figure 5(J)). This implies that, during RILF progression, the secretory activity of fibroblasts undergoing ferroptosis increases, consequently accelerating the fibrotic advancement of RILF.

Discussion

RILF affects the efficacy of radiotherapy, leading to a decreased prognosis and affecting the quality of life in patients with thoracic tumors.[26] However, research on the mechanism of RILF is ongoing, and there are currently no better therapeutic strategies.[29,37] We established a mouse model of RILF to investigate the underlying mechanisms. Our analysis of transcriptome microarray data revealed certain pathways related to oxidative stress, inflammatory responses, iron ion metabolism, and lipid peroxidation, which is in line with earlier research.[8,10,11,38,39] These pathways indicated ferroptosis occurred in RILF.

Ferroptosis, a newly described form of regulated necrosis characterized by an increase in the production of deleterious lipid ROS through iron-dependent lipid peroxidation, is distinct from apoptosis and necrosis and has been recognized as a major form of cell death.[40-42] Recent studies have increasingly shown a close relationship between fibrosis and ferroptosis in cells. For instance, research by Guo et al utilizing liver organoid cultures identified the critical role of NCOA4 in mediating ferroptosis in fibroblasts, which is significant for the progression of liver fibrosis.[43] Similarly, Zhang et al demonstrated that the use of liproxstatin-1 (lip-1) inhibits RSL3-induced ferroptosis in HK2 cells. This inhibition also reduced the secretion of pro-fibrotic factors by HK2 cells, thereby ameliorating renal fibrosis.[44] Additionally, in their study on endometriosis, Zhang et al[45] found that ferric ammonium citrate (FAC) induces ferroptosis in cells, exacerbating fibrosis.[45] However, the role of ferroptosis in RILF remains less studied, and its specific mechanisms are still unclear.

To investigate this, we used the KEGG ferroptosis-related gene set to develop an FRG score to evaluate ferroptosis in RILF. In the irradiated lung tissue of mice, a notable positive correlation was observed between the FRG scores and scores related to collagen, fibrosis, inflammation, and other ECM components. This implies that ferroptosis is involved in the progression of RILF.[8]

Subsequently, we sought to identify specific cells that primarily undergo ferroptosis, thereby promoting the progression of fibrosis. We employed sc-RNAseq data for RILF and computed FRG scores for all cells. Our investigation revealed that the FRG scores of fibroblasts and epithelial cells varied significantly between the IR and control groups. We hypothesized that changes in ferroptosis in these two cell types contributed to the development of fibrosis. Li et al. observed that human alveolar epithelial cells secrete large amounts of cytokines, or inflammatory factors.[11] These inflammatory factors attract macrophages, prompting their polarization and further release of cytokines such as TGF-β, which contribute to the epithelial–mesenchymal transition in epithelial cells, as well as the endothelial–mesenchymal transition in endothelial cells, causing a series of pro-fibrotic responses downstream.[46,47] Cell damage and fibrosis were alleviated by treatment with Fer-1.[10,11]

The elevation of FRG scores in fibroblasts is an interesting phenomenon. We extracted fibroblasts and subclassified them and found that myofibroblasts had a more pronounced FRG score elevation. The ability of the cells to secrete ECM was assessed using the ECM score, and the Myofibroblast ECM score was correspondingly higher after irradiation. To substantiate our findings, we assessed fibroblasts using gene sets associated with iron and lipid metabolism. Our analysis revealed elevated scores for both gene sets in myofibroblasts, indicating that metabolic pathways related to ferroptosis may significantly contribute to the transition from fibroblasts to myofibroblasts.

The dysregulation of iron-dependent lipid peroxidation is an important feature of ferroptosis, which is also an inducing factor for fibroblast activation. By inducing lipid peroxidation in human lung fibroblasts with TGF-β, Yue Gong et al. revealed that cellular lipid peroxidation plays a stimulatory role in fibroblast activation.[48] Zhuo Pei et al observed that in a bleomycin-induced mouse model of pulmonary fibrosis, TGF-β influenced the concentration of intracellular iron ions by regulating transferrin receptor (TFRC). This regulation affects iron ion metabolism and lipid peroxidation. The synergistic effects of these processes contributed to fibroblast activation.[49] ACSL4 is a key enzyme involved in the process of lipid peroxidation and is a marker commonly indicative of ferroptosis. PDGFRα is one of the markers of fibroblast to myofibroblast transformation.[36] We used immunofluorescence co-staining for ACSL4 and PDGFRα and found an increase in co-stained cells in the fibrotic region after IR, proving our conjecture that the ferroptosis-related pathway in RILI plays an important role in the activation of fibroblasts.[50]

In our RILF model, we noted an elevation in the FRG score along with heightened pathways associated with lipid and iron metabolism in myofibroblasts. The formation of myofibroblasts is a manifestation of fibroblast activation. X-ray irradiation directly leads to the accumulation of intracellular ROS, as well as damage to epithelial and endothelial cells, and the damaged cells secrete IL-1, IL16, and TGF-β. These factors recruit macrophages, further causing the release of a large number of pro-fibrotic cytokines, such as TGF-β, which act on the fibroblast to promote its activation and the secretion of ECM to promote the development of fibrosis.

Simultaneously, the direct impact of X-rays on fibroblasts leads to the intracellular dysregulation of lipid metabolism, increased ROS levels, and disruption of GSH metabolism, implying that the cells undergo ferroptosis. These reactions may directly contribute to cell activation, thereby prompting

the transformation into myofibroblasts. Activated myofibroblasts, in turn, secrete ECM components, including collagen, further promoting lung fibrosis.

A limitation of our study was the absence of supplementary in vitro investigations into X-ray-induced fibroblast activation through the activation of ferroptosis-related pathways. Subsequently, we plan to conduct a comprehensive study to explore the genetic alterations and intrinsic cellular metabolism of fibroblasts undergoing ferroptosis.

Conclusion

In conclusion, our research indicated that in RILF, fibroblasts undergoing ferroptosis may release increased levels of ECM, potentially accelerating the progression of lung fibrosis. This finding presents ferroptosis as a potential therapeutic target in RILF.

Declaration of Conflicting Interests

The author(s) declared no potential conflicts of interest with respect to the research, authorship, and/or publication of this article.

Funding

The author(s) disclosed receipt of the following financial support for the research, authorship, and/or publication of this article: This work was supported by the National Nature Science Foundation of China (grant number 82273576).

Ethical Statement

Ethical Approval

The animal experiments were carried out in accordance with ethical procedures and the protocol was approved by the Ethics Committee of Nanfang Hospital, Southern Medical University (approval number: NFEC-2020-033).

ORCID iD

Minying Li https://orcid.org/0009-0002-0487-6336

Supplemental Material

Supplemental material for this article is available online.

References

1. Coggle JE, Lambert BE, Moores SR. Radiation effects in the lung. *Environ Health Perspect*. 1986;70:261-291. doi:10.1289/ehp.8670261
2. Tsoutsou PG, Koukourakis MI. Radiation pneumonitis and fibrosis: mechanisms underlying its pathogenesis and implications for future research. *Int J Radiat Oncol*. 2006;66(5):1281-1293. doi:10.1016/j.ijrobp.2006.08.058
3. Mehta V. Radiation pneumonitis and pulmonary fibrosis in non–small-cell lung cancer: pulmonary function, prediction, and prevention. *Int J Radiat Oncol*. 2005;63(1):5-24. doi:10.1016/j.ijrobp.2005.03.047
4. Marks L, Yu X, Vujaskovic Z, Small W, Folz R, Anscher M. Radiation-induced lung injury. *Semin Radiat Oncol*. 2003;13(3):333-345. doi:10.1016/S1053-4296(03)00034-1
5. Fleckenstein K, Zgonjanin L, Chen L, et al. Temporal onset of hypoxia and oxidative stress after pulmonary irradiation. *Int J Radiat Oncol*. 2007;68(1):196-204. doi:10.1016/j.ijrobp.2006.12.056
6. Ding NH, Li J, Sun LQ. Molecular mechanisms and treatment of radiation-induced lung fibrosis. *Curr Drug Targets*. 2013;14(11):1347-1356. doi:10.2174/13894501113149990198
7. Dixon SJ, Lemberg KM, Lamprecht MR, et al. Ferroptosis: an iron-dependent form of nonapoptotic cell death. *Cell*. 2012;149(5):1060-1072. doi:10.1016/j.cell.2012.03.042
8. Li X, Zhuang X, Qiao T. Role of ferroptosis in the process of acute radiation-induced lung injury in mice. *Biochem Biophys Res Commun*. 2019;519(2):240-245. doi:10.1016/j.bbrc.2019.08.165
9. Li X, Chen J, Yuan S, Zhuang X, Qiao T. Activation of the P62-keap1-NRF2 pathway protects against ferroptosis in radiation-induced lung injury. *Oxid Med Cell Longev*. 2020;2022:8973509. doi:10.1155/2022/8973509
10. Li X, Duan L, Yuan S, Zhuang X, Qiao T, He J. Ferroptosis inhibitor alleviates Radiation-induced lung fibrosis (RILF) via down-regulation of TGF-β1. *J Inflamm*. 2019;16(1):11. doi:10.1186/s12950-019-0216-0
11. Li L, Wu D, Deng S, et al. NVP-AUY922 alleviates radiation-induced lung injury via inhibition of autophagy-dependent ferroptosis. *Cell Death Dis*. 2022;8(1):86. doi:10.1038/s41420-022-00887-9
12. Curras-Alonso S, Soulier J, Defard T, et al. An interactive murine single-cell atlas of the lung responses to radiation injury. *Nat Commun*. 2023;14(1):2445. doi:10.1038/s41467-023-38134-z
13. Ritchie ME, Phipson B, Wu D, et al. Limma powers differential expression analyses for RNA-sequencing and microarray studies. *Nucleic Acids Res*. 2015;43(7):e47. doi:10.1093/nar/gkv007
14. Consortium TGO. Gene ontology consortium: going forward. *Nucleic Acids Res*. 2015;43(D1):D1049-D1056. doi:10.1093/nar/gku1179
15. The gene ontology: enhancements for 2011. *Nucleic Acids Res*. 2012;40(D1):D559-D564. doi:10.1093/nar/gkr1028
16. Gene ontology annotations and resources. *Nucleic Acids Res* 2013;41(D1):D530-D535. doi:10.1093/nar/gks1050
17. Ashburner M, Ball CA, Blake JA, et al. Gene ontology: tool for the unification of biology. The Gene Ontology Consortium. *Nat Genet*. 2000;25(1):25-29. doi:10.1038/75556
18. Kanehisa M, Furumichi M, Sato Y, Ishiguro-Watanabe M, Tanabe M. KEGG: integrating viruses and cellular organisms. *Nucleic Acids Res*. 2021;49(D1):D545-D551. doi:10.1093/nar/gkaa970
19. Kanehisa M, Goto S. KEGG: Kyoto Encyclopedia of genes and genomes. *Nucleic Acids Res*. 2000;28(1):27-30. doi:10.1093/nar/28.1.27
20. Hao Y, Hao S, Andersen-Nissen E, et al. Integrated analysis of multimodal single-cell data. *Cell*. 2021;184(13):3573-3587.e29. doi:10.1016/j.cell.2021.04.048

21. Wu T, Hu E, Xu S, et al. clusterProfiler 4.0: a universal enrichment tool for interpreting omics data. *Innovation*. 2021;2(3):100141. doi:10.1016/j.xinn.2021.100141
22. Citrin DE, Shankavaram U, Horton JA, et al. Role of type II pneumocyte senescence in radiation-induced lung fibrosis. *J Natl Cancer Inst*. 2013;105(19):1474-1484. doi:10.1093/jnci/djt212
23. Liberzon A, Birger C, Thorvaldsdóttir H, Ghandi M, Mesirov JP, Tamayo P. The Molecular Signatures Database (MSigDB) hallmark gene set collection. *Cell Syst*. 2015;1(6):417-425. doi:10.1016/j.cels.2015.12.004
24. Hänzelmann S, Castelo R, Guinney J. GSVA: gene set variation analysis for microarray and RNA-Seq data. *BMC Bioinf*. 2013;14(1):7. doi:10.1186/1471-2105-14-7
25. Zhou C, Jones B, Moustafa M, et al. Quantitative assessment of radiation dose and fractionation effects on normal tissue by utilizing a novel lung fibrosis index model. *Radiat Oncol*. 2017;12(1):172. doi:10.1186/s13014-017-0912-y
26. Bledsoe TJ, Nath SK, Decker RH. Radiation pneumonitis. *Clin Chest Med*. 2017;38(2):201-208. doi:10.1016/j.ccm.2016.12.004
27. Käsmann L, Dietrich A, Staab-Weijnitz CA, et al. Radiation-induced lung toxicity – cellular and molecular mechanisms of pathogenesis, management, and literature review. *Radiat Oncol*. 2020;15(1):214. doi:10.1186/s13014-020-01654-9
28. Roy S, Salerno KE, Citrin DE. Biology of radiation-induced lung injury. *Semin Radiat Oncol*. 2021;31(2):155-161. doi:10.1016/j.semradonc.2020.11.006
29. Hanania AN, Mainwaring W, Ghebre YT, Hanania NA, Ludwig M. Radiation-induced lung injury: assessment and management. *Chest*. 2019;156(1):150-162. doi:10.1016/j.chest.2019.03.033
30. Dong Z, Li T, Wang C, et al. Lipid peroxidation and iron metabolism: two corner stones in the homeostasis control of ferroptosis. *Int J Mol Sci*. 2023;24(1):449. doi:10.3390/ijms24010449
31. Wang Y, Liao S, Pan Z, et al. Hydrogen sulfide alleviates particulate matter-induced emphysema and airway inflammation by suppressing ferroptosis. *Free Radic Biol Med*. 2022;186:1-16. doi:10.1016/j.freeradbiomed.2022.04.014
32. Wang K, Li Z, Ding Y, et al. Ferritinophagy-mediated ferroptosis is involved in sepsis-induced cardiac injury. *Free Radic Biol Med*. 2020;160:303-318. doi:10.1016/j.freeradbiomed.2020.08.009
33. Tong J, Lan X, Zhang Z, et al. Ferroptosis inhibitor liproxstatin-1 alleviates metabolic dysfunction-associated fatty liver disease in mice: potential involvement of PANoptosis. *Acta Pharmacol Sin*. 2023;44(5):1014-1028. doi:10.1038/s41401-022-01010-5
34. Das A, Meng W, Liu Z. SnapShot: ferroptosis. *Cell*. 2020;181(5):1188-1188.e1. doi:10.1016/j.cell.2020.04.039
35. Morgan GW, Pharm B, Breit SN. Radiation and the lung: a reevaluation of the mechanisms mediating pulmonary injury. *Int J Radiat Oncol*. 1995;31(2):361-369. doi:10.1016/0360-3016(94)00477-3
36. Dong Z, Li T, Wang C, et al. Temporal control of PDGFRα regulates the fibroblast-to-myofibroblast transition in wound healing. *Cell Rep*. 2022;40(7):111192. doi:10.1016/j.celrep.2022.111192
37. Cherian SV, Patel D, Machnicki S, et al. Algorithmic approach to the diagnosis of organizing pneumonia: a correlation of clinical, radiologic, and pathologic features. *Chest*. 2022;162(1):156-178. doi:10.1016/j.chest.2021.12.659
38. Dong H, Xia Y, Jin S, et al. Nrf2 attenuates ferroptosis-mediated IIR-ALI by modulating TERT and SLC7A11. *Cell Death Dis*. 2021;12(11):1027. doi:10.1038/s41419-021-04307-1
39. Zhang J, Li K, Zhang Q, Zhu Z, Huang G, Tian H. Polycysteine as a new type of radio-protector ameliorated tissue injury through inhibiting ferroptosis in mice. *Cell Death Dis*. 2021;12(2):195. doi:10.1038/s41419-021-03479-0
40. Lu LQ, Tian J, Luo XJ, Peng J. Targeting the pathways of regulated necrosis: a potential strategy for alleviation of cardiocerebrovascular injury. *Cell Mol Life Sci*. 2021;78(1):63-78. doi:10.1007/s00018-020-03587-8
41. Minagawa S, Yoshida M, Araya J, Hara H, Imai H, Kuwano K. Regulated necrosis in pulmonary disease. A focus on necroptosis and ferroptosis. *Am J Respir Cell Mol Biol*. 2020;62(5):554-562. doi:10.1165/rcmb.2019-0337TR
42. Mou Y, Wang J, Wu J, et al. Ferroptosis, a new form of cell death: opportunities and challenges in cancer. *J Hematol Oncol*. 2019;12(1):34. doi:10.1186/s13045-019-0720-y
43. Guo J, Duan L, He X, et al. A combined model of human iPSC-derived liver organoids and hepatocytes reveals ferroptosis in DGUOK mutant mtDNA depletion syndrome. *Adv Sci*. 2021;8(10):2004680. doi:10.1002/advs.202004680
44. Zhang B, Chen X, Ru F, et al. Liproxstatin-1 attenuates unilateral ureteral obstruction-induced renal fibrosis by inhibiting renal tubular epithelial cells ferroptosis. *Cell Death Dis*. 2021;12(9):843. doi:10.1038/s41419-021-04137-1
45. Zhang Y, Liu X, Deng M, et al. Ferroptosis induced by iron overload promotes fibrosis in ovarian endometriosis and is related to subpopulations of endometrial stromal cells. *Front Pharmacol*. 2022;13:930614. doi:10.3389/fphar.2022.930614
46. Kim KK, Kugler MC, Wolters PJ, et al. Alveolar epithelial cell mesenchymal transition develops *in vivo* during pulmonary fibrosis and is regulated by the extracellular matrix. *Proc Natl Acad Sci USA*. 2006;103(35):13180-13185. doi:10.1073/pnas.0605669103
47. Kalluri R, Weinberg RA. The basics of epithelial-mesenchymal transition. *J Clin Invest*. 2009;119(6):1420-1428. doi:10.1172/JCI39104
48. Gong Y, Wang N, Liu N, Dong H. Lipid peroxidation and GPX4 inhibition are common causes for myofibroblast differentiation and ferroptosis. *DNA Cell Biol*. 2019;38(7):725-733. doi:10.1089/dna.2018.4541
49. Bai YT, Chang R, Wang H, Xiao FJ, Ge RL, Wang LS. ENPP2 protects cardiomyocytes from erastin-induced ferroptosis. *Biochem Biophys Res Commun*. 2018;499(1):44-51. doi:10.1016/j.bbrc.2018.03.113
50. Pei Z, Qin Y, Fu X, et al. Inhibition of ferroptosis and iron accumulation alleviates pulmonary fibrosis in a bleomycin model. *Redox Biol*. 2022;57:102509. doi:10.1016/j.redox.2022.102509